

# High electron mobility and quantum oscillations in non-encapsulated ultrathin semiconducting Bi<sub>2</sub>O<sub>2</sub>Se

Jinxiong Wu<sup>1†</sup>, Hongtao Yuan<sup>2,3,4†</sup>, Mengmeng Meng<sup>5</sup>, Cheng Chen<sup>6</sup>, Yan Sun<sup>7,8</sup>, Zhuoyu Chen<sup>3</sup>, Wenhui Dang<sup>1</sup>, Congwei Tan<sup>1</sup>, Yujing Liu<sup>1</sup>, Jianbo Yin<sup>1</sup>, Yubing Zhou<sup>1</sup>, Shaoyun Huang<sup>5</sup>, H. Q. Xu<sup>5</sup>, Yi Cui<sup>3,4</sup>, Harold Y. Hwang<sup>3,4</sup>, Zhongfan Liu<sup>1</sup>, Yulin Chen<sup>6</sup>, Binghai Yan<sup>7,8</sup> and Hailin Peng<sup>1\*</sup>

**High-mobility semiconducting ultrathin films form the basis of modern electronics, and may lead to the scalable fabrication of highly performing devices. Because the ultrathin limit cannot be reached for traditional semiconductors, identifying new two-dimensional materials with both high carrier mobility and a large electronic bandgap is a pivotal goal of fundamental research<sup>1–9</sup>. However, air-stable ultrathin semiconducting materials with superior performances remain elusive at present<sup>10</sup>. Here, we report ultrathin films of non-encapsulated layered Bi<sub>2</sub>O<sub>2</sub>Se, grown by chemical vapour deposition, which demonstrate excellent air stability and high-mobility semiconducting behaviour. We observe bandgap values of ~0.8 eV, which are strongly dependent on the film thickness due to quantum-confinement effects. An ultrahigh Hall mobility value of >20,000 cm<sup>2</sup> V<sup>-1</sup> s<sup>-1</sup> is measured in as-grown Bi<sub>2</sub>O<sub>2</sub>Se nanoflakes at low temperatures. This value is comparable to what is observed in graphene grown by chemical vapour deposition<sup>11</sup> and at the LaAlO<sub>3</sub>-SrTiO<sub>3</sub> interface<sup>12</sup>, making the detection of Shubnikov-de Haas quantum oscillations possible. Top-gated field-effect transistors based on Bi<sub>2</sub>O<sub>2</sub>Se crystals down to the bilayer limit exhibit high Hall mobility values (up to 450 cm<sup>2</sup> V<sup>-1</sup> s<sup>-1</sup>), large current on/off ratios (>10<sup>6</sup>) and near-ideal subthreshold swing values (~65 mV dec<sup>-1</sup>) at room temperature. Our results make Bi<sub>2</sub>O<sub>2</sub>Se a promising candidate for future high-speed and low-power electronic applications.**

As a typical bismuth-based oxychalcogenide material, layered Bi<sub>2</sub>O<sub>2</sub>Se shows a tetragonal structure with *I4/mmm* space group (*a* = 3.88 Å, *c* = 12.16 Å and *Z* = 2), and consists of planar covalently bonded oxide layers (Bi<sub>2</sub>O<sub>2</sub>) sandwiched by Se square arrays with relatively weak electrostatic interactions (Fig. 1a and Supplementary Fig. 1)<sup>13</sup>. Layered Bi<sub>2</sub>O<sub>2</sub>Se lacks standard van der Waals gaps, unlike other two-dimensional semiconductors<sup>14,15</sup> (for details see Supplementary Section I), resulting in intriguing cleavage along Se planes and possible rearrangement of the surface atomic structure. We studied the band structure and density of states of bulk Bi<sub>2</sub>O<sub>2</sub>Se crystals by both first-principles calculations (Fig. 1b and Supplementary Fig. 2) and angle-resolved photoemission spectroscopy (ARPES) measurements (Fig. 1c–e). The electronic states near the conduction band minimum at the *Γ* point originate mainly from the Bi *p*-orbital bands and disperse strongly along the *Γ*-*X* and *Γ*-*M* directions, which host

three-dimensional features sensitive to thickness. This can cause a size-tunable bandgap upon thinning towards the monolayer limit, due to the effects of quantum confinement (Supplementary Figs 2–4). An indirect bandgap of ~0.8 eV was clearly revealed by ARPES, consistent with the calculated value of ~0.85 eV (Fig. 1b,d). Importantly, we obtained a very low in-plane electron effective mass of  $m^* = 0.14 \pm 0.02m_0$  ( $m_0$  is the free-electron mass) by fitting the conduction band mapped out by ARPES (for more details see Fig. 1e and Supplementary Fig. 5). Note that this  $m^*$  value is lower than the values for silicon ( $0.26m_0$ ), MoS<sub>2</sub> ( $0.4$ – $0.6m_0$ )<sup>6,16</sup> and black phosphorus ( $0.15m_0$  for  $m_x^*$ ,  $1.18m_0$  for  $m_y^*$ )<sup>17</sup> and thus suggests the possibility of achieving ultrahigh electron mobility, as demonstrated in the following.

Because of its unique layered structure, Bi<sub>2</sub>O<sub>2</sub>Se preferentially crystallizes into ultrathin two-dimensional crystals with a large lateral size on a suitable substrate during chemical vapour deposition (CVD) growth. Here, sub-millimetre single-crystalline Bi<sub>2</sub>O<sub>2</sub>Se nanoplates were synthesized on atomically flat fluorophlogopite mica via van der Waals epitaxy (see Methods)<sup>18,19</sup>. As shown in Fig. 2a,b and Supplementary Fig. 6, as-grown Bi<sub>2</sub>O<sub>2</sub>Se nanoplates with a square shape and ultraflat surfaces exhibit a very large single-domain size of over  $0.2 \times 0.2$  mm<sup>2</sup> and thicknesses of ~6.7 nm (corresponding to ~11 layers, as confirmed by atomic force microscopy (AFM), Fig. 2c). The profile of the terraced Bi<sub>2</sub>O<sub>2</sub>Se nanoplates reveals a step height of ~0.6 nm, consistent with the 0.61 nm of the known Bi<sub>2</sub>O<sub>2</sub>Se crystal structure (Fig. 1a and Supplementary Fig. 7), suggesting a layer-by-layer or edge growth mode. Remarkably, the monolayer Bi<sub>2</sub>O<sub>2</sub>Se nanoplates (~0.8 nm) exhibit lateral dimensions greater than 40 μm in some cases (Fig. 2d and Supplementary Fig. 8), implying the potential to achieve a wafer size suitable for practical applications. The single-crystalline nature of two-dimensional layered Bi<sub>2</sub>O<sub>2</sub>Se and its tetragonal *I4/mmm* space group were further confirmed by X-ray diffraction (XRD) patterns (Fig. 2e), transmission electron microscopy (TEM, Fig. 2f–h) images, selected area electron diffraction (SAED) patterns (Fig. 2g, inset) and energy-dispersive X-ray spectroscopy (EDS) element mapping images (Fig. 2i–l and Supplementary Fig. 9). More importantly, the surface morphology and roughness of ultrathin Bi<sub>2</sub>O<sub>2</sub>Se crystals remain almost the same, even after exposure to air for months, indicative of their excellent environmental stability (Supplementary Figs 10 and 11).

<sup>1</sup>Center for Nanochemistry, Beijing National Laboratory for Molecular Sciences (BNLMS), College of Chemistry and Molecular Engineering, Peking University, Beijing 100871, China. <sup>2</sup>National Laboratory of Solid-State Microstructures, College of Engineering and Applied Sciences, and Collaborative Innovation Center of Advanced Microstructures, Nanjing University, Nanjing 210093, China. <sup>3</sup>Geballe Laboratory for Advanced Materials, Stanford University, Stanford, California 94305, USA. <sup>4</sup>Stanford Institute for Materials and Energy Sciences, SLAC National Accelerator Laboratory, Menlo Park, California 94025, USA. <sup>5</sup>Key Laboratory for the Physics and Chemistry of Nanodevices, Department of Electronics, Peking University, Beijing 100871, China. <sup>6</sup>Department of Physics and Clarendon Laboratory, University of Oxford, Parks Road, Oxford OX1 3PU, UK. <sup>7</sup>Max Planck Institute for Chemical Physics of Solids, D-01187 Dresden, Germany. <sup>8</sup>School of Physical Science and Technology, ShanghaiTech University, Shanghai 200031, China. <sup>†</sup>These authors contributed equally to this work. \*e-mail: [hlpeng@pku.edu.cn](mailto:hlpeng@pku.edu.cn)

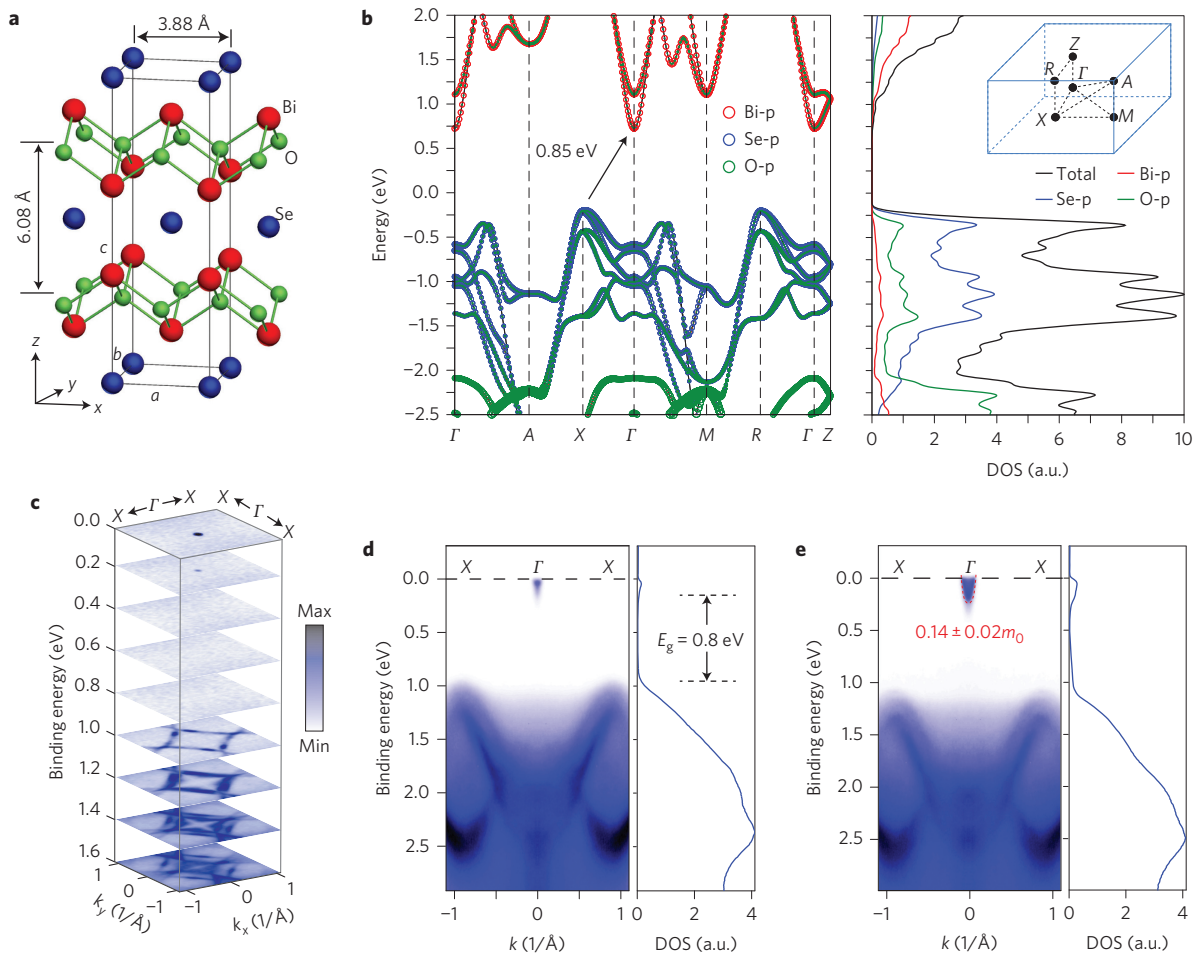


**Figure 1 | Lattice and electronic structure of layered  $\text{Bi}_2\text{O}_2\text{Se}$ .** **a**, Layered crystal structure of  $\text{Bi}_2\text{O}_2\text{Se}$  with tetragonal  $(\text{Bi}_2\text{O}_2)_n$  layers and  $\text{Se}_n$  layers alternately stacked along the  $c$  axis. For clarity, the weak electrostatic interactions between Se and the  $[\text{Bi}_2\text{O}_2]$  layer in  $\text{Bi}_2\text{O}_2\text{Se}$  are not presented. **b**, Calculated band structure and density of states (DOS) of  $\text{Bi}_2\text{O}_2\text{Se}$  with a bandgap of  $\sim 0.85$  eV. The inset in the right panel is the first Brillouin zone of  $\text{Bi}_2\text{O}_2\text{Se}$ . **c, d**, Band structure and DOS of bulk  $\text{Bi}_2\text{O}_2\text{Se}$  observed by ARPES measurements. An indirect bandgap of  $\sim 0.8$  eV is clearly observable. **e**, Band dispersions of the conduction band and DOS measured after surface K-doping to lift the chemical potential, revealing a low effective mass of  $0.14 \pm 0.02m_0$ .

As-grown air-stable high-quality  $\text{Bi}_2\text{O}_2\text{Se}$  flakes on mica were fabricated directly into standard Hall-bar devices (processing without inert gas protection) for the evaluation of carrier mobility. As shown in Fig. 3a and Supplementary Fig. 12, the electron Hall mobility of non-encapsulated  $\text{Bi}_2\text{O}_2\text{Se}$  flakes reached values of  $18,500\text{--}28,900 \text{ cm}^2 \text{ V}^{-1} \text{ s}^{-1}$  at 1.9 K. The long mean free path of the ultrahigh-mobility electrons enabled the observation of Shubnikov–de Haas (SdH) quantum oscillations (Fig. 3b). From a Fourier transform of the clear SdH oscillations in terms of  $1/B$  for the range  $4 \text{ T} < B < 14 \text{ T}$  (Supplementary Fig. 13a), three frequencies were identified. Nominal peak assignments by Lorentzian fitting gave the three primary components at 43.4, 58.2 and 120 T (Supplementary Fig. 13b). These frequencies correspond to respective sheet carrier densities,  $n_{\text{SdH}}$ , of  $2.1 \times 10^{12} \text{ cm}^{-2}$ ,  $2.8 \times 10^{12} \text{ cm}^{-2}$  and  $5.8 \times 10^{12} \text{ cm}^{-2}$  (representing 0.16, 0.21 and 0.44% of the Brillouin zone, respectively) based on the free electron approximation and a twofold spin degeneracy. The total sum of  $n_{\text{SdH}}$  is consistent with the sheet carrier density of  $1.1 \times 10^{13} \text{ cm}^{-2}$  derived from the Hall effect. Note that this  $\text{Bi}_2\text{O}_2\text{Se}$  sample displays a moderate room-temperature mobility of  $\sim 150 \text{ cm}^2 \text{ V}^{-1} \text{ s}^{-1}$  with a relatively high carrier density, indicating that there is a substantial room for further optimization to achieve samples with even higher mobility by reducing the carrier density.

To estimate the in-plane cyclotron effective mass  $m^*$  of the mobile electrons, we analysed the temperature-dependence of the

SdH oscillation amplitude  $\Delta R$  in perpendicular magnetic fields (Fig. 3b and Supplementary Fig. 14), where quantum oscillatory features persist to temperatures as high as 30 K. The normalized amplitudes at 12.8 T were fitted using the Lifshitz–Kosevich formula

$$\frac{\Delta R}{R_0} = \exp\left(\frac{-4\pi^3 k_B T_D}{h\omega_c}\right) \frac{16\pi^3 k_B T/h\omega_c}{\sinh(4\pi^3 k_B T/h\omega_c)} \quad (1)$$

where  $R_0$  is the resistance when the oscillation is absent,  $k_B$  is the Boltzmann constant,  $h$  is Planck's constant,  $T_D$  is the Dingle temperature,  $\omega_c = eB/m^*$  is the cyclotron frequency, and  $m^*$  and  $B$  are the in-plane effective mass of mobile electrons and the magnetic flux density, respectively. The fit shown in Fig. 3c gives an  $m^*$  value as small as  $0.14 \pm 0.02m_0$ , which is consistent with the theoretical prediction and the results of angle-resolved photoemission spectroscopy.

Such large-area ultrathin  $\text{Bi}_2\text{O}_2\text{Se}$  crystals with low effective mass and large bandgap facilitate the fabrication of high-performance electronic devices. In the top-gated  $\text{Bi}_2\text{O}_2\text{Se}$  field-effect transistor (FET) (channel thickness of 6.2 nm), Pd/Au metal electrodes were used to create ohmic contacts with linear behaviour in the source–drain current ( $I_{\text{ds}}$ ) as a function of bias ( $V_{\text{ds}}$ ) (Fig. 4a and Supplementary Fig. 14). The room-temperature transfer characteristics show ambipolar operation with a superior  $I_{\text{on}}/I_{\text{off}}$  of  $\sim 10^6$  for electron accumulation (Fig. 4b and Supplementary Figs 15–17),

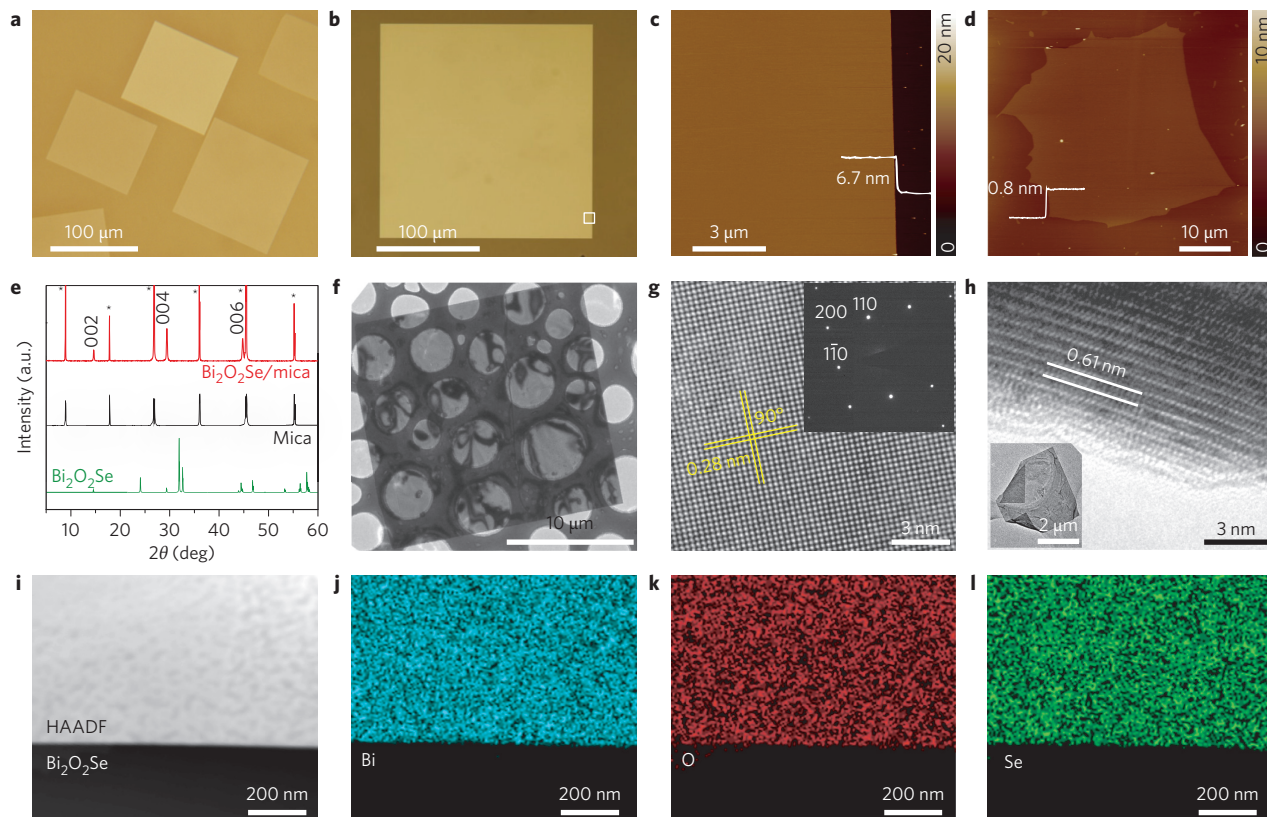


**Figure 2 | Growth and characterization of layered  $\text{Bi}_2\text{O}_2\text{Se}$  nanoplates.** **a**, Typical optical microscopy image of square  $\text{Bi}_2\text{O}_2\text{Se}$  nanoplates grown on mica via van der Waals epitaxy. **b**, Optical microscopy image of a  $\text{Bi}_2\text{O}_2\text{Se}$  nanoplate with a domain size larger than  $200\ \mu\text{m}$ . **c**, Corresponding AFM image recorded at the rectangular area highlighted in **b**. **d**, AFM image of monolayer  $\text{Bi}_2\text{O}_2\text{Se}$  with a domain size larger than  $40\ \mu\text{m}$ , showing a thickness of  $\sim 0.8\ \text{nm}$ . **e**, XRD pattern of  $\text{Bi}_2\text{O}_2\text{Se}$  nanoplates grown on mica (red) with a reference blank mica substrate (black) and the simulated diffractogram (green). The lattice planes indexed as (002), (004) and (006) agree well with a reference diffractogram of single-phase tetragonal  $\text{Bi}_2\text{O}_2\text{Se}$  ( $I4/mmm$ ,  $a = 3.88\ \text{\AA}$  and  $c = 12.16\ \text{\AA}$ ), indicating the pure phase of layered  $\text{Bi}_2\text{O}_2\text{Se}$ . The asterisks indicate signal from the mica substrate. **f**, TEM image of a square  $\text{Bi}_2\text{O}_2\text{Se}$  nanoplate. **g**, High-resolution (HR) TEM image of the  $\text{Bi}_2\text{O}_2\text{Se}$  nanoplate. The SAED pattern (inset) shows that the nanoplate is single-crystalline. **h**, HRTEM image recorded from the folded edge of a  $\text{Bi}_2\text{O}_2\text{Se}$  nanoplate (inset), showing a lattice spacing of  $0.61\ \text{nm}$ , consistent with the layer height of tetragonal  $\text{Bi}_2\text{O}_2\text{Se}$ . **i-l**, High-angle annular dark-field (HAADF) image of a  $\text{Bi}_2\text{O}_2\text{Se}$  nanoplate (**i**) and corresponding elemental maps for Bi (**j**), O (**k**) and Se (**l**).

which significantly exceeds the level of  $10^4$  for practical logic transistors<sup>20,21</sup>. The steep current drop clearly indicates low subthreshold swing values ( $\sim 65\ \text{mV dec}^{-1}$ , shown in Fig. 4b, approaching the limit of  $60\ \text{mV dec}^{-1}$  at  $300\ \text{K}$  for conventional metal–oxide–semiconductor FETs) and high electron mobility, both of which are key metrics for high-speed and low-power logic devices<sup>4</sup>.

Figure 4c shows the estimated room-temperature apparent field-effect mobility ( $\mu_{\text{app}}$ ) as a function of gate voltage ( $V_g$ ) using the  $dI_{\text{ds}}/dV_g$  differential based on the equation

$$\mu_{\text{app}} = \frac{L}{W} \frac{1}{C_g} \frac{dI_{\text{ds}}}{V_{\text{ds}} dV_g} \quad (2)$$

where  $C_g$  is the top gate oxide capacitance, and  $L$  and  $W$  are the channel length and width. Interestingly,  $\mu_{\text{app}}$  increases gradually and reaches high values ( $>1,500\ \text{cm}^2\ \text{V}^{-1}\ \text{s}^{-1}$ ) as  $V_g$  scans to negative voltages for electron depletion (Fig. 4c). Such a dramatic increase of mobility with decreasing  $V_g$  implies the reduction of the scattering events due to the envelope wavefunction centre of mass for electrons being pushed away from the  $\text{Bi}_2\text{O}_2\text{Se}$  surface. More importantly, as shown in the evolution of mobility with thickness (the  $\mu_{\text{app}}$  obtained from linear fitting, Fig. 4d, and Supplementary Fig. 15),  $\mu_{\text{app}}$  maintains high values of over  $2,000\ \text{cm}^2\ \text{V}^{-1}\ \text{s}^{-1}$  for thicker samples but begins to drop dramatically when the sample thickness is less than  $6\ \text{nm}$ , while the  $I_{\text{on}}/I_{\text{off}}$  ratio increases monotonically from  $\sim 10^3$  to  $\sim 10^6$  as the channel thickness decreases. These observations

clearly suggest that the suppression of electron scattering at the surface/interface is crucial to further improve the device performance of ultrathin  $\text{Bi}_2\text{O}_2\text{Se}$ .

The  $\mu_{\text{app}}$  values in two-probe FET configurations are strongly dependent on  $V_g$  (Fig. 4c), which might suggest a possible overestimation of  $\mu_{\text{app}}$  near the threshold voltage (for details see Supplementary Section VIII)<sup>22–25</sup>. We therefore also performed Hall-effect measurements to accurately demonstrate carrier mobility as a function of  $\text{Bi}_2\text{O}_2\text{Se}$  thickness down to a bilayer (Fig. 4e and Supplementary Fig. 17). The room-temperature Hall mobility ( $\mu_{\text{Hall}}$ ) of top-gated  $\text{Bi}_2\text{O}_2\text{Se}$  samples (Fig. 4e) maintained an almost constant value of  $\sim 200\ \text{cm}^2\ \text{V}^{-1}\ \text{s}^{-1}$  for thicker  $\text{Bi}_2\text{O}_2\text{Se}$  samples, but dropped suddenly for samples with a thickness below  $6.2\ \text{nm}$ . This observation, ascribed to a severer surface/interface scattering in ultrathin  $\text{Bi}_2\text{O}_2\text{Se}$  flakes, is consistent with the scenario for thickness-dependent  $\mu_{\text{app}}$ . Such an interface scattering mechanism can be further demonstrated by the temperature-dependent sheet resistance ( $R_{\text{xx}}$ ) of  $\text{Bi}_2\text{O}_2\text{Se}$  flakes with different thicknesses. The bilayer sample exhibits more interface scattering and a localization behaviour (a dramatic resistance upturn when cooling below  $70\ \text{K}$ ), while thicker samples (heavily n-doped semiconductor) show metallic behaviour (Fig. 4f)<sup>25,26</sup>.

The maximum Hall mobility of CVD-grown  $\text{Bi}_2\text{O}_2\text{Se}$  flakes is as high as  $\sim 450\ \text{cm}^2\ \text{V}^{-1}\ \text{s}^{-1}$  at room temperature and  $\sim 29,000\ \text{cm}^2\ \text{V}^{-1}\ \text{s}^{-1}$  at  $1.9\ \text{K}$ , and both values are expected to have substantial room for further optimization with growth

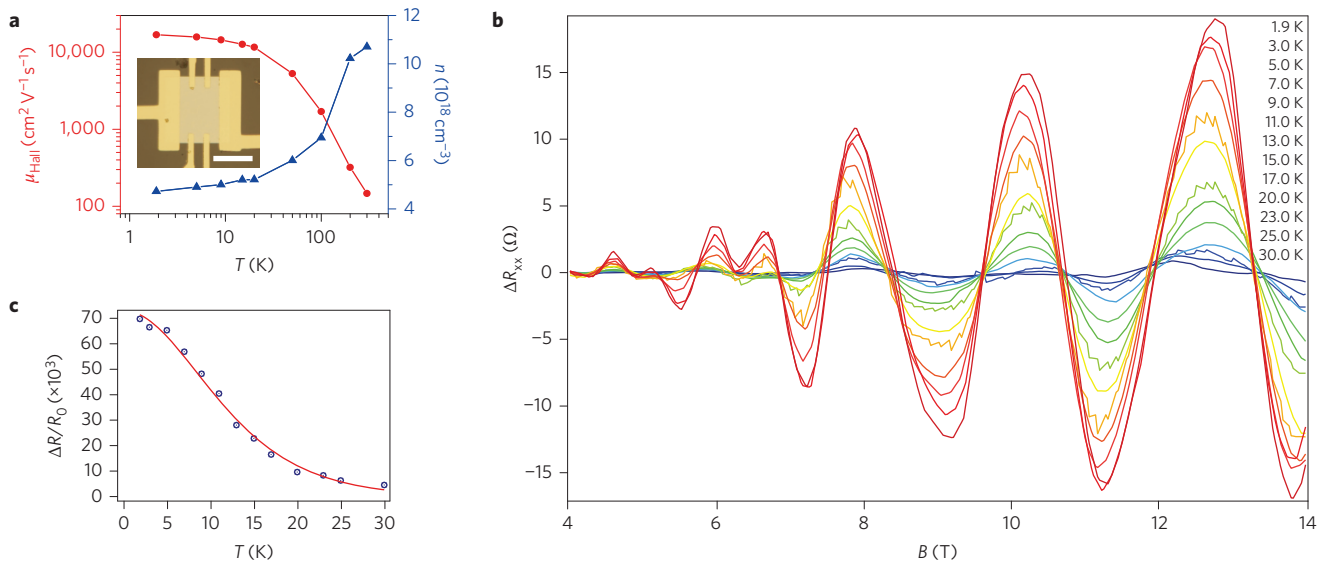


**Figure 3 | Shubnikov-de Haas quantum oscillations in non-encapsulated  $\text{Bi}_2\text{O}_2\text{Se}$  crystals.** **a**, Hall mobility ( $\mu_{\text{Hall}}$ ) and carrier density ( $n$ ) as a function of temperature in a  $\text{Bi}_2\text{O}_2\text{Se}$  nanoplate. Inset: optical microscopy image of a Hall-bar device fabricated on the  $\text{Bi}_2\text{O}_2\text{Se}$  nanoplate with a thickness of  $\sim 20.9$  nm. The Hall mobility of this particular device is  $18,500 \text{ cm}^2 \text{V}^{-1} \text{s}^{-1}$  at 1.9 K. Scale bar,  $20 \mu\text{m}$ . **b**, SdH oscillatory part of the longitudinal magnetoresistance  $\Delta R_{xx}$  as a function of applied perpendicular magnetic field measured in the temperature range from 1.9 to 30 K. The non-oscillatory part was removed by subtracting a high-tolerance smoothing spline fit. **c**, Temperature-dependent  $\Delta R/R_0$  values of the SdH oscillations and the Lifshitz-Kosevich fitting at 12.8 T, giving a low cyclotron in-plane effective mass of  $0.14 \pm 0.02 m_0$ .

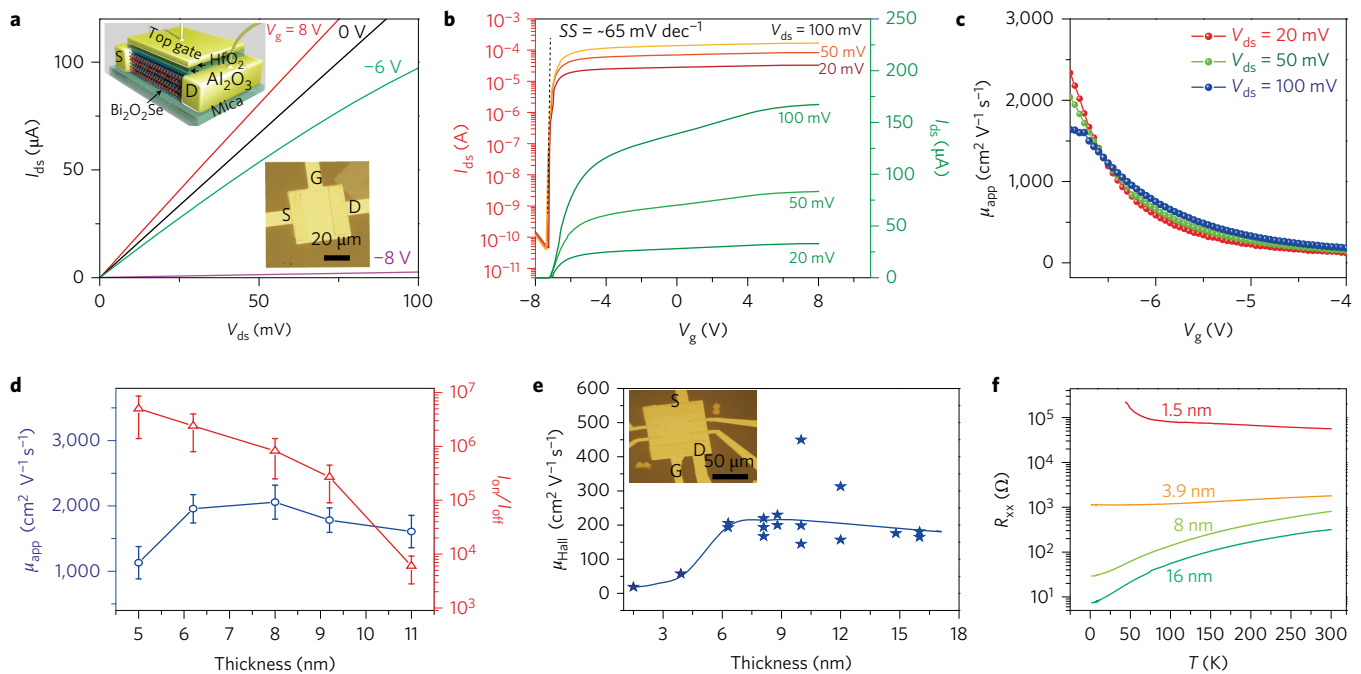


**Figure 4 | Room-temperature mobility of top-gated  $\text{Bi}_2\text{O}_2\text{Se}$ -channel FETs with large on/off ratios.** **a**, Output curves obtained from a 6.2-nm-thick  $\text{Bi}_2\text{O}_2\text{Se}$  device at room temperature. Inset: schematic of the device structure (upper plane) and optical microscopy image of a top-gated device (bottom plane) directly fabricated on a thick mica substrate ( $\sim 200 \mu\text{m}$ ), with 5 nm  $\text{Al}_2\text{O}_3$  and 20 nm  $\text{HfO}_2$  serving as the single top-gate dielectrics. **b**, Top-gate transfer curves ( $I_{\text{ds}} - V_{\text{g}}$ ) of the device with different source-drain voltages (100, 50, 20 mV), exhibiting a large on/off ratio of  $\sim 10^6$  and a near ideal subthreshold swing (SS) value of  $\sim 65 \text{ mV dec}^{-1}$ .  $I_{\text{ds}}$  is shown on a logarithmic scale (left) and a non-logarithmic scale (right). **c**, Apparent field-effect mobility ( $\mu_{\text{app}}$ ) (extracted from the differential of  $dI_{\text{ds}}/dV_{\text{g}}$ ) as a function of gate voltage with different bias voltages (20, 50, 100 mV). **d**,  $\mu_{\text{app}}$  and  $I_{\text{on}}/I_{\text{off}}$  of  $\text{Bi}_2\text{O}_2\text{Se}$  FETs as a function of channel thickness, where  $\mu_{\text{app}}$  was extracted from the linear fitting of transfer curves. Error bars arise from the uncertainty in determining the linear-fitting transconductance of the transfer curves and mobility discrepancy on different devices. **e**, Statistics for the room-temperature Hall mobility of CVD-grown  $\text{Bi}_2\text{O}_2\text{Se}$  as a function of flake thickness, which varies from 1.5 to 16 nm. **f**, Temperature-dependent resistance measurements for  $\text{Bi}_2\text{O}_2\text{Se}$  with different channel thicknesses.

control, gate tuning and surface encapsulation with hexagonal boron nitride (h-BN)<sup>27,28</sup>. The ultrahigh mobility characteristics of Bi<sub>2</sub>O<sub>2</sub>Se may be more generally applicable to other bismuth oxychalcogenide members (Bi<sub>2</sub>O<sub>2</sub>S and Bi<sub>2</sub>O<sub>2</sub>Te) with tunable bandgap sizes<sup>29,30</sup>. Thus, the presented air-stable ultrahigh-mobility layered Bi<sub>2</sub>O<sub>2</sub>Se semiconductor could open a new avenue to connect the previously disparate worlds of high-mobility semiconductors and low-cost CVD growth. In particular, as we approach the few-layer two-dimensional limit, its high mobility, as well as its chemical stability and easy accessibility, make Bi<sub>2</sub>O<sub>2</sub>Se a promising candidate for realizing novel quantum phenomena, future logic devices and flexible electronics applications.

## Methods

Methods and any associated references are available in the [online version of the paper](#).

Received 8 March 2016; accepted 20 February 2017;  
published online 3 April 2017

## References

- Reich, E. S. Phosphorene excites materials scientists. *Nature* **506**, 19 (2014).
- Li, L. *et al.* Black phosphorus field-effect transistors. *Nat. Nanotech.* **9**, 372–377 (2014).
- Radisavljevic, B., Radenovic, A., Brivio, J., Giacometti, V. & Kis, A. Single-layer MoS<sub>2</sub> transistors. *Nat. Nanotech.* **6**, 147–150 (2011).
- Fiori, G. *et al.* Electronics based on two-dimensional materials. *Nat. Nanotech.* **9**, 768–779 (2014).
- Novoselov, K. S. *et al.* Electric field effect in atomically thin carbon films. *Science* **306**, 666–669 (2004).
- Li, S.-L., Tsukagoshi, K., Orgiu, E. & Samori, P. Charge transport and mobility engineering in two-dimensional transition metal chalcogenide semiconductors. *Chem. Soc. Rev.* **45**, 118–151 (2016).
- Zhang, Y., Tan, Y.-W., Stormer, H. L. & Kim, P. Experimental observation of the quantum Hall effect and Berry's phase in graphene. *Nature* **438**, 201–204 (2005).
- Novoselov, K. S. *et al.* Two-dimensional gas of massless Dirac fermions in graphene. *Nature* **438**, 197–200 (2005).
- Li, L. *et al.* Quantum Hall effect in black phosphorus two-dimensional electron system. *Nat. Nanotech.* **11**, 593–597 (2016).
- Island, J. O., Steele, G. A., van der Zant, H. S. & Castellanos-Gomez, A. Environmental instability of few-layer black phosphorus. *2D Mater.* **2**, 011002 (2015).
- Li, X. *et al.* Large-area synthesis of high-quality and uniform graphene films on copper foils. *Science* **324**, 1312–1314 (2009).
- Ohtomo, A. & Hwang, H. A high-mobility electron gas at the LaAlO<sub>3</sub>/SrTiO<sub>3</sub> heterointerface. *Nature* **427**, 423–426 (2004).
- Boller, H. Crystal structure of Bi<sub>2</sub>O<sub>2</sub>Se. *Monatsh. Chem.* **104**, 916–919 (1973).
- Nicolosi, V., Chhowalla, M., Kanatzidis, M. G., Strano, M. S. & Coleman, J. N. Liquid exfoliation of layered materials. *Science* **340**, 1226419 (2013).
- Geim, A. K. & Grigorieva, I. V. Van der Waals heterostructures. *Nature* **499**, 419–425 (2013).
- Zhang, W. X., Huang, Z. S., Zhang, W. L. & Li, Y. R. Two-dimensional semiconductors with possible high room temperature mobility. *Nano Res.* **7**, 1731–1737 (2014).
- Qiao, J., Kong, X., Hu, Z.-X., Yang, F. & Ji, W. High-mobility transport anisotropy and linear dichroism in few-layer black phosphorus. *Nat. Commun.* **5**, 4475 (2014).
- Li, H. *et al.* Controlled synthesis of topological insulator nanoplate arrays on mica. *J. Am. Chem. Soc.* **134**, 6132–6135 (2012).
- Peng, H. *et al.* Topological insulator nanostructures for near-infrared transparent flexible electrodes. *Nat. Chem.* **4**, 281–286 (2012).
- Schwierz, F. Graphene transistors. *Nat. Nanotech.* **5**, 487–496 (2010).
- Wang, Q. H., Kalantar-Zadeh, K., Kis, A., Coleman, J. N. & Strano, M. S. Electronics and optoelectronics of two-dimensional transition metal dichalcogenides. *Nat. Nanotech.* **7**, 699–712 (2012).
- Bittle, E. G., Basham, J. I., Jackson, T. N., Jurchescu, O. D. & Gundlach, D. J. Mobility overestimation due to gated contacts in organic field-effect transistors. *Nat. Commun.* **7**, 10908 (2016).
- Uemura, T. *et al.* On the extraction of charge carrier mobility in high-mobility organic transistors. *Adv. Mater.* **28**, 151–155 (2016).
- Fuhrer, M. S. & Hone, J. Measurement of mobility in dual-gated MoS<sub>2</sub> transistors. *Nat. Nanotech.* **8**, 146–147 (2013).
- Radisavljevic, B. & Kis, A. Mobility engineering and a metal–insulator transition in monolayer MoS<sub>2</sub>. *Nat. Mater.* **12**, 815–820 (2013).
- Kim, Y. S. *et al.* Thickness-dependent bulk properties and weak antilocalization effect in topological insulator Bi<sub>2</sub>Se<sub>3</sub>. *Phys. Rev. B* **84**, 073109 (2011).
- Cui, X. *et al.* Multi-terminal transport measurements of MoS<sub>2</sub> using a van der Waals heterostructure device platform. *Nat. Nanotech.* **10**, 534–540 (2015).
- Wang, L. *et al.* One-dimensional electrical contact to a two-dimensional material. *Science* **342**, 614–617 (2013).
- Zhang, X. *et al.* Thermal decomposition of bismuth oxysulfide from photoelectric Bi<sub>2</sub>O<sub>2</sub>S to superconducting Bi<sub>4</sub>O<sub>4</sub>S<sub>3</sub>. *ACS Appl. Mater. Inter.* **7**, 4442–4448 (2015).
- Luu, S. D. & Vaqueiro, P. Synthesis, characterisation and thermoelectric properties of the oxytelluride Bi<sub>2</sub>O<sub>2</sub>Te. *J. Solid State Chem.* **226**, 219–223 (2015).

## Acknowledgements

The authors thank X. B. Ren and C. H. Jin for analysis of elemental maps. H.L.P. acknowledges support from the National Basic Research Program of China (grant numbers 2014CB932500 and 2016YFA0200101), the National Natural Science Foundation of China (grant number 21525310) and the National Program for Support of Top-Notch Young Professionals. H.T.Y., Y.C. and H.Y.H. were supported by the Department of Energy, Office of Basic Energy Sciences, Division of Materials Sciences and Engineering, under contract number DE-AC02-76SF00515.

## Author contributions

H.P., J.W. and H.T.Y. conceived the original idea for the project. J.W. carried out the synthesis and structural characterizations of the bulk and two-dimensional crystals. The devices were fabricated by J.W. with M.M.'s help. H.T.Y., J.W., M.M., J.Y. and Z.C. performed the transport measurements and data analysis. Y.S. and Y.B. carried out the theoretical calculations. The ARPES measurements were done by C.C. and Y.L.C. The manuscript was written by H.P., H.T.Y. and J.W., with input from the other authors. All work was supervised by H.P. All authors contributed to the scientific planning and discussions.

## Additional information

Supplementary information is available in the [online version of the paper](#). Reprints and permissions information is available online at [www.nature.com/reprints](http://www.nature.com/reprints). Publisher's note: Springer Nature remains neutral with regard to jurisdictional claims in published maps and institutional affiliations. Correspondence and requests for materials should be addressed to H.P.

## Competing financial interests

The authors declare no competing financial interests.

## Methods

**CVD growth and characterization of Bi<sub>2</sub>O<sub>2</sub>Se nanoplates.** Two-dimensional Bi<sub>2</sub>O<sub>2</sub>Se crystals were synthesized inside a home-made low-pressure CVD system equipped with a 12 inch horizontal tube furnace and 30-mm-diameter quartz tube. As source materials, Bi<sub>2</sub>O<sub>3</sub> powder (Alfa Aesar, 5 N) and Bi<sub>2</sub>Se<sub>3</sub> bulk (Alfa Aesar, 5 N) were placed in the hot centre and upstream by 5 cm for evaporation, respectively. Argon was used as the carrier gas to transport the vapour precursor to the cold region (9–12 cm downstream), where growth substrates of freshly cleaved fluorophlogopite mica were located. Typical growth conditions were as follows. The source temperature was 580–650 °C, and the growth substrate temperature was ~500–550 °C. The system pressure was in the range 100–400 torr and the carrier gas flow rate was ~100–200 s.c.c.m. Growth time ranged from 10 to 60 min.

For characterization of the as-grown Bi<sub>2</sub>O<sub>2</sub>Se nanoplates, we performed optical microscopy (OM, Olympus DX51 microscope), atomic force microscopy (AFM, Bruker Dimension Icon with Nanoscope V controller), X-ray diffraction (XRD, Rigaku Dmax 2500 PC, Cu K $\alpha$  radiation with 40 kV and 100 mA) and transmission electron microscopy (TEM, FEI Tecnai F30, acceleration voltage 300 kV for bright-field high-resolution TEM and HAADF-STEM-EDS measurements). The samples were transferred onto the lacey carbon film supported copper grids for TEM characterization with a dilute HF solution (2%).

**Growth of Bi<sub>2</sub>O<sub>2</sub>Se bulk crystals.** Single crystals of bulk Bi<sub>2</sub>O<sub>2</sub>Se were prepared using a modified Bridgman method. Stoichiometric high-purity Bi<sub>2</sub>O<sub>3</sub> powder (99.999%), Se powder (99.999%) and Bi powder (99.999%) were weighed into an evacuated quartz tube with pressure down to 10<sup>-2</sup> Pa. Bi<sub>2</sub>O<sub>2</sub>Se powder was obtained by maintaining the temperature at 773 K for 6 h. As-synthesized Bi<sub>2</sub>O<sub>2</sub>Se powder was melted at 1,223 K for 2 h, then slowly cooled to 1,003 K over 24 h and maintained at 1,003 K for 48 h, then finally cooled to room temperature to form a bulk crystal, which was confirmed to be tetragonal Bi<sub>2</sub>O<sub>2</sub>Se with space group *I4/mmm* (*a* = 3.88 Å, *c* = 12.16 Å, *Z* = 2) by XRD.

**First-principles calculations.** To resolve the band structure of Bi<sub>2</sub>O<sub>2</sub>Se, we first performed first-principles calculations for Bi<sub>2</sub>O<sub>2</sub>Se. Density functional theory (DFT) calculations were performed using the Vienna *ab initio* simulation package (VASP) with core electrons represented by the projector-augmented-wave (PAW) potential<sup>31</sup>. To obtain accurate band structures, the modified Becke–Johnson exchange potential<sup>32</sup> was adopted for the exchange–correlation functional. A *k*-point grid of 35 × 35 × 13 was used for Brillouin zone sampling. The effective masses of  $m_{xx}^{\text{eff}}$  and  $m_{zz}^{\text{eff}}$  were derived by fitting the energy dispersions along the *k<sub>x</sub>* and *k<sub>z</sub>* directions in the lowest conduction bands, respectively. The energy window from 0.0 to 0.1 eV above the conduction band minimum (CBM) around the  $\Gamma$  point was used in parabolic fitting. The Fermi velocity was calculated from  $v_F^i = (\partial E_F / \hbar \partial k_{F,i})$ , with  $E_F$  lying 0.1 eV above the CBM, and *i* = *x* and *z*. The Fermi velocities along the

*x* and *z* directions are  $v_F^x = 4.4 \times 10^5$  m s<sup>-1</sup> and  $v_F^z = 1.3 \times 10^5$  m s<sup>-1</sup>, respectively, and the effective masses along the *x* and *z* directions are  $m_{xx}^{\text{eff}} = 0.18 m_0$  and  $m_{zz}^{\text{eff}} = 0.47 m_0$ , respectively.

**Angle-resolved photoemission spectroscopy (ARPES).** The band structure of Bi<sub>2</sub>O<sub>2</sub>Se was further confirmed experimentally by ARPES. The ARPES experiments were performed on the Bi<sub>2</sub>O<sub>2</sub>Se bulk crystals at beamline I05 of the Diamond Light Source (DLS). Data were recorded by a Scienta R4000 analyser with total convolved energy and angle resolutions of 20 meV and 0.2°, respectively. During the experiment, the sample was maintained in an ultrahigh-vacuum system under a pressure lower than 1 × 10<sup>-10</sup> torr, and the sample temperature was kept at 10 K. A fresh surface of Bi<sub>2</sub>O<sub>2</sub>Se single crystal was obtained for ARPES measurements by cleaving the sample *in situ* along its natural (001) cleavage plane.

**Device fabrication and electrical transport measurements.** Both Hall bar devices of individual Bi<sub>2</sub>O<sub>2</sub>Se nanoplates and the top-gate field-effect transistors (FETs) were fabricated directly on as-grown nanoplates on an insulating mica substrate. Alignment marker arrays were first predefined onto the mica with standard photolithography techniques. Electron-beam lithography (EBL) was then used to write multiple metal contacts for both six-terminal Hall-bar structures and the two-terminal FETs. Ohmic contact was formed using Pd/Au metal electrodes (8 nm/60 nm). The fabrication of top-gated FETs requires a second-step EBL process, followed by atomic layer deposition to grow the high- $\kappa$  top-gate dielectrics of Al<sub>2</sub>O<sub>3</sub> (5 nm) and HfO<sub>2</sub> (20 nm). Note that two layers of photoresist (conductive protective coating SX AR-PC-5000 and poly(methyl methacrylate)) were used to prevent charge accumulation on the insulating mica substrate during EBL.

Transport measurements were performed in two- and four-probe configurations in two different physical properties measurement systems (PPMS, Quantum Design) with superconducting magnets of up to 9 and 14 T, respectively. The temperature ranged from 1.9 to 400 K. The magnetic field was always applied perpendicular to the devices. Electrical measurement of top-gate FET behaviour was carried out on a semiconductor analyser (Keithley, SCS-4200) combined with a micromanipulator 6200 probe station at room temperature under ambient conditions.

**Data availability.** The data supporting the findings of this study are available within the paper and its Supplementary Information.

## References

- Kresse, G. & Furthmüller, J. Efficient iterative schemes for *ab initio* total-energy calculations using a plane-wave basis set. *Phys. Rev. B* **54**, 11169 (1996).
- Tran, F. & Blaha, P. Accurate band gaps of semiconductors and insulators with a semilocal exchange–correlation potential. *Phys. Rev. Lett.* **102**, 226401 (2009).